Nanoscale

Accepted Manuscript

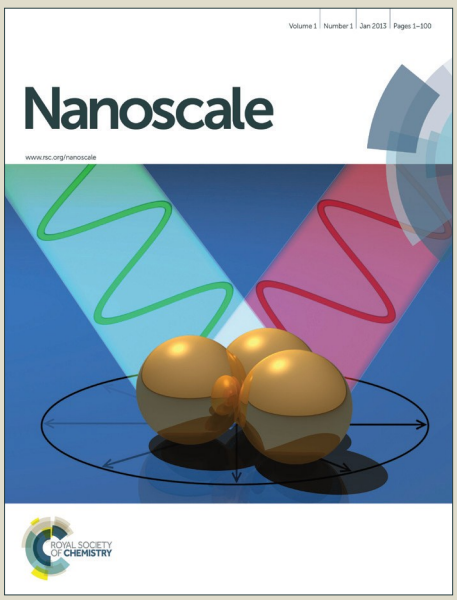

ROYAL SOCIETY OF CHEMISTRY

www.rsc.org/nanoscale

Nanoscale

ARTICLE

Tailorable Chiroptical Activity of Metallic Nanospiral arrays

J. H. Deng,[a,e] J. Ng[a-c] and Z. F. Huang[*a,c-e]

Received 00th January 20xx,
Accepted 00th January 20xx

DOI: 10.1039/x0xx00000x

www.rsc.org/

It is in its infancy to engineer chiroptical activity of an emerging chiral metamaterial, metallic nanospirals. We utilize glancing angle deposition (GLAD) to facilely sculpture the helical structure of silver nanospirals (AgNSs), such that the scope of chiroptical engineering factors is broadened to include the spiral growth of homochiral AgNSs, the combination of left- and right-handed helical chirality to create heterochiral AgNSs, and the coil-axis alignment of the heterochiral AgNSs. It leads to flexible control over chiroptical activity of AgNS arrays with respect to the sign, resonance wavelength and amplitude of circular dichroism (CD) in the UV and visible regime. The UV chiroptical mode has distinct response from the visible mode. Finite element simulation together with the LC circuit theory illustrates that the UV irradiation is mainly adsorbed in the metal and the visible is preferentially scattered by AgNSs, accounting for the wavelength-related chiroptical distinction. This work contributes to broadening the horizons to understand and engineer chiroptical responses, primarily desired to develop a wide range of potential chiroplasmonic applications.

Introduction

Chirality describes an asymmetric property that an object cannot be superimposed onto its mirror image. In spite of mysterious origin, chirality does naturally exist from the macro to atomic scale. The incorporation of structural chirality renders plasmonic materials become chiroptically active, leading to some cutting-edge, chiroplasmon-induced applications such as the ultrasensitive DNA detection.[1] Chiroptical activity is usually characterized by, but not limited to, CD[2] that evaluates the difference in optical extinction of left- and right-handed circularly polarized irradiation (LCP and RCP) by a sample.[3] Two kinds of approaches have been developed to create chiroptical materials. One is to chemically conjugate chiral molecules (i.e., enantiomers) with achiral nanostructures to induce chiroptical response in the nanostructures;[1, 4-20] Another is to physically generate chiral metamaterials without the conjugation with enantiomers, including multi-layer chiral stacking,[21-25] and the generation of chiral metamaterials in the two-dimensional (2D)[26-28] and 3D.[29, 30] 3D chiral metamaterials have intrinsic, strong chiroptical activity decoupling from supporting substrates, so at to catch an increasing attention to fundamentally understand and engineer the inherent chiroptical activity, as a prerequisite to explore potential chiroplasmonic applications.

3D chiral metamaterials typically have a helical profile. Plasmonic microspirals, fabricated by direct laser writing,[29] radio frequency plasma prior to electroless plating,[31] and multi-beam holographic lithography,[32] have a helical pitch (*P*, inset in Fig. 1) in the micrometer scale and exhibit chiroptical response in the IR spectrum. Plasmonic NSs with a sub-micrometer pitch are chiroptically active in the UV-visible-near IR spectrum.[33] It has been reported on four NS-fabrication methods, including colloidal nanohole lithography,[34] focused ion beam induced deposition,[35] electron beam induced deposition[36] and GLAD.[30] The 1st NS-fabrication method inevitably contains a series of pre- and post-fabrication processes; the 2nd and 3rd have a practical difficulty in large-area fabrication. In that sense, GLAD is a unique technique to operate one-step-process, wafer-scale production and enables one to facilely sculpture helical structures and engineer spiral materials.[37, 38] Although dielectric NSs were successfully created by GLAD to study chiroptical response in ~20 years ago,[39, 40] it is challenging to sculpture noble metals to be NSs. It is primarily ascribed to that noble metals have relatively low melting point, resulting in uncontrollable surface diffusion of metallic adatoms after kinetically adhering to an existing NS. In 2013 Fischer *et al.* used liquid N_2 to cool the substrate to -170 ^{0}C under which the surface diffusion of adatoms can be significantly prohibited, and demonstrated GLAD of Au NSs with *P* of ~30 nm.[30] Presently, to our best knowledge, only a few groups are capable of employing GLAD to generate plasmonic NSs and commence to engineer chiroptical

[a] *Department of Physics, Hong Kong Baptist University (HKBU), Kowloon Tong, Kowloon, Hong Kong SAR, P. R. China.*
[b] *Institute of Computational and Theoretical Studies, HKBU, Kowloon Tong, Kowloon, Hong Kong SAR, P. R. China.*
[c] *Institute of Advanced Materials, HKBU, Kowloon Tong, Kowloon, Hong Kong SAR, P. R. China.*
[d] *Partner State Key Laboratory of Environmental and Biological Analysis, HKBU, Kowloon Tong, Kowloon, Hong Kong SAR, P. R. China.*
[e] *HKBU Institute of Research and Continuing Education, 9F, the Industrialization Complex of Shenzhen Virtual University Park, No.2 Yuexing 3rd Road, South Zone, Hi-tech Industrial Park, Nanshan District, Shenzhen, Guangdong Province, P. R. China*
Email:zfhuang@hkbu.edu.hk
Electronic Supplementary Information (ESI) available: FEM, LC circuit theory, CD of homochiral co-3L and co-3R AgNS arrays, and the fractional-pitch growth of heterochiral bi- and co-axial AgNS arrays. See DOI: 10.1039/x0xx00000x

activity.[41-43] Chiroptical response is substantially governed by helical materials and structures (characterized by spiral pitch *P*, the number of pitch *n*, height *H* (*H*=*nP*), coil diameter *D* and wire diameter *d*).[44] To measure CD, NSs are either dispersed in a solvent or assembled in an array on a transparent substrate. CD of dispersed Au NSs is amplified with *n* in the visible spectrum.[30] For a hexagonal array of Cu NSs having a fixed *H*, with an increase of *P* and *D* the visible CD tends to redshift, broaden in linewidth and rise in amplitude,[41] as predicted by the numerical simulation.[45] The *P*-induced red shift also occurs in the Ti-Ag alloy NS array.[42] For a hexagonal array of Au-Ag alloy NSs, a shrinkage of the inter-NS spacing from 80 to 50 nm causes the UV-visible CD redshift and increase in chiroptical amplitude,[41] probably ascribed to the plasmonic coupling.[46, 47] The resonant wavelength of CD can be flexibly tuned in the entire visible spectrum by engineering spiral materials, e.g. ~750 nm for Cu, ~600 nm for Au and ~480 nm for Cu-Ag and Ni-Ag alloys.[33]

Compared to the dispersed NSs, a NS array is more practically preferential to explore chiroptical applications. It is in an early stage, however, to investigate chiroptical principle and control chiroptical activity of plasmonic NS arrays. Herein, we study the chiroptical evolution with the full-pitch growth of a homochiral AgNS array, which is simulated by finite element method (FEM) and the LC circuit model (L-electric inductance; C-electric capacitance) to study chiroptical principle. Chiroptical activity is further modulated by integrating the left- and right-handed helical chirality to generate heterochiral AgNSs, and by engineering the alignment of the two incorporated helix longitudinal axes. It will obtain new horizons to understand and control chiroptical activity of plasmonic NS arrays.

Experimental

GLAD

In a custom-built physical vapor deposition chamber (JunSun Tech Co. Ltd., Taiwan), GLAD was operated at a deposition angle of 86^0 (with respect to the substrate normal) and in a high vacuum of 10^{-7}-10^{-6} Torr. Ag powders (99.99%, Kurt J. Lesker) were evaporated to deposit on Si wafers (Semiconductor Wafer, Inc.) and sapphires (MTL, Hong Kong) in an area of 1.5×1.5 cm^2. The deposition rate (R_d) was controlled to be 3 Å/s monitored by a quartz crystal microbalance, at an electron-beam accelerating voltage of 8.0 kV and emission current of 15-25 mA. Substrate temperature was controlled to be ~2 ^{0}C by an ethanol cooling system, except for the deposition of five-pitch homochiral AgNSs at ~(-40) ^{0}C. As-deposited Ag was sculptured in the helical by rotating substrates: the clockwise rotation generates the right-handed and the counter-clockwise produces the left-handed. *P* (in unit of nm per revolution) can be engineered by

$$P = 360\, R_d/R_r \qquad (1)$$

where R_r is the substrate rotation rate (in unit of degree per second). R_d was calibrated as 0.67 Å/s with respect to the glancing deposition angle of 86^0. In this work, *P* was fixed as 200 nm, such that a substrate was rotated at 0.12 deg/s accordingly. *n* can be facilely engineered by the azimuthal angle (φ) of substrate rotation: φ of 120^0, 240^0, 360^0, 720^0, 1080^0 and 1800^0 generates *n* of 1/3, 2/3, 1, 2, 3 and 5, respectively. The homochiral co-axial AgNSs were generated via the unidirectional rotation of a substrate in *n* circles. To create the heterochiral bi-axial AgNSs, after the first full-circle rotation the substrate was immediately rotated in a direction opposite to that of the first circle. For the heterochiral co-axial AgNSs, after the first full-circle rotation the substrate was quickly rotated in φ of 180^0 before the subsequent, opposite-direction rotation. Without surface pre-pattern, GLAD enables one to deposit a close-packed, random array of vertical AgNSs.

CD

It was monitored CD of an AgNS array deposited on a sapphire, in the wavelength of 300-700 nm (Olis 1000 CD, Fig. 2a). LCP and RCP were incident along the normal of the sapphire. To avoid linear birefringence and linear dichroism, a sample was continuously rotated at 0.1 rpm to subsequently detect five CD spectra that were algebraically averaged to obtain an average CD spectrum.

Structural characterization

An as-deposited substrate was mechanically split, leaving the freshly split surface for SEM characterization (field emission scanning electron microscopy, Oxford, LEO 1530).

FEM and LC circuit theory

FEM was operated using the commercial software package of "Comsol Multi-physics". FEM and LC circuit theory was elaborated in ESI.

Results and discussion

Homochiral co-axial AgNS arrays

Homochiral co-axial AgNSs are composed of one or multiple full-pitch (*n*: 1 (Figs. 1a-b), 2 (Figs. 1c-d) and 3 (Figs. 1e-f)) that have mono-chirality (in left-handed (Figs. 1a, c, e: in red) or right-handed (Figs. 1b, d, f: in blue)) and grow along a longitudinal coil axis. It is denoted as co-nL and co-nR AgNSs, where co-, *n*, L and R represent the co-axial, the number of pitch, left-handed and right-handed, respectively. Fig. 2b shows CD of a homochiral co-axial array with tailorable *n*, in which the CD amplitude (i.e., ellipticity) is normalized by *n*. With switching the helical handedness, the CD spectrum flips along the zero CD. At *n* of 1, the CD spectrum is composed of two bisignated peaks, one is in the UV regime and another is in the visible. The UV chiroptical mode barely varies with *n*, in terms of the *n*-normalized ellipticity and peak position. For the visible chiroptical mode, on the contrary, an increase of *n* significantly reduces the *n*-normalized ellipticity, makes the visible peak split into two bisignated peaks, and causes the one with shorter resonant wavelength blueshift. It is indicated that the UV mode chiroptically differs from the visible one.

To understand the wavelength-related chiroptical distinction, FEM is utilized to numerically simulate CD of an individual homochiral co-axial AgNS under an incidence along the helix longitudinal axis (see ESI S1). In the simulation, optical interaction involves the scattering (i.e., radiative loss characterized by radiative resistance R_{rad}, since the loss power is proportional to electric resistance at a given current) and absorption (i.e., Ohmic loss within the metal characterized by Ohmic resistance R_{ohm}). The simulation illustrates that the radiative loss (or R_{rad}) dominates in the visible spectrum, but has a contribution comparable to the Ohmic loss (or R_{ohm}) in the UV regime (Fig. 2c). The LC circuit theory (see ESI S2) shows that the *n*-normalized ellipticity can be evaluated by R_{rad}/n in a reciprocal manner (eqn (S2-6) and eqn (S2-8)). When $n<1$, R_{rad}/n quickly increases with *n* (Fig. 2d). R_{rad}/n of the UV chiroptical mode appears to increase faster than that of the visible, and reaches a maximum plateau when $n>1$. It accounts for the decoupling of the *n*-normalized UV ellipticity from *n* in the range of 1-3. In the same range of *n*, R_{rad}/n of the visible mode continuously increases with *n*, leading to the gradual decrease in the *n*-normalized visible ellipticity. The visible mode tends to has a maximized R_{rad}/n at $n>3$, accounting for that the *n*-normalized visible ellipticity saturates when *n* rises from 3 to 5 (Fig. S1). It is difficult to simulate chiroptical response of the as-deposited close-packed, random array. However, the simulation of individual AgNS explains very well the chiroptical dependence of a random array on *n*, indicating that the single-spiral simulation does extract the intrinsic chiroptical principle of a random array.

It is extracted from the FEM simulation the distribution of the scattering electric field E_{sca} excited by the UV and visible circularly polarized incidence (Figs. 3a-c). Fig. 3d shows a plot of circumferentially integrated scattering intensity ($|E_{sca}|^2$) normalized by the incident intensity, versus a radius *r* pointing from the center of a coil cross-section. It is illuminated that outside AgNS the visible light causes more scattering energy than the UV since the visible has a longer wavelength, whereas inside the metal the UV has a smaller extinction coefficient to extend further into the metal than the visible. As a result, more UV energy is localized inside the metal than the visible, while more visible energy is scattered than the UV. It accounts for the wavelength-related chiroptical distinction. Note that coil cross-sections (e.g. the one in Fig. 3a) have been arbitrarily selected in the co-3L AgNS simulate, and the analogous results are obtained.

Heterochiral bi-axial and co-axial AgNS arrays

Remarkably, GLAD enables one to tailor chiroptical activity via the incorporation of the left and right-handed helixes to form heterochiral AgNSs, as well as via the control over the alignment of the two incorporated helix longitudinal axes. It is deposited a heterochiral bi-(1L+1R) array (Fig. 4a) and its mirror image bi-(1R+1L) (Fig. 4b), where "bi-" represents the bi-axial structure with the mis-alignment of the two incorporated helix longitudinal axes. It is intriguingly found out that the visible CD mode (composed of two bisignated peaks, separated at ~550 nm) flips in sign with switching the direction of optical incidence, but the UV mode doesn't (Figs. 4c-d). It is further illuminated the wavelength-related chiroptical distinction, and illustrated that the heterochiral bi-axial array can function as a circular polarizer in the visible regime by simply rotating the array to switch the incident direction. Interestingly, when the two longitudinal axes are aligned (i.e., the fabrication of heterochiral co-axial array, Figs. 5a-b), it is effectively eliminated the function of the visible circular polarizer induced by switching the incident direction (Figs. 5c-d). Analogously, a homochiral co-axial array doesn't change in the CD sign with switching the incident direction (Fig. S2), illustrating that the circular polarizer function mainly stems from the hetero-axial mis-alignment.

After switching the incident direction, the CD spectrum fails to overlap with the original one regardless of the CD sign (Figs. 4-5), that is, the incident direction-related chiroptical asymmetry. It is probably ascribed to the extinguishing achiral nanoparticles (e.g. Figs. 5a-b). The GLAD process is dominated by the self-shadowing and competing effect, leading to the extinguishing of small nanoparticles located in the shadow regions of the growing AgNSs.[48] The extinguishing nanoparticles attach to the substrate without growing into AgNSs, and are buried in the AgNS array. Consequently, they tend to be invisible under the frontward incidence but emerge under the backward incidence. As a result, the incident direction-related chiroptical asymmetry originates from the structural asymmetry with respect to the supporting substrate.

Unexpectedly, the hetero-chirality incorporation doesn't extinguish the chiroptical activity. To understand it, we study the chiroptical evolution with the fractional-pitch growth of the upper spiral (Figs. 6-7), by depositing a series of heterochiral arrays of bi-(1L+nR), bi-(1R+nL), co-(1L+nR) and co-(1R+nL) with *n* of 0, 1/3, 2/3 and 1 (Figs. S3-S4). For the heterochiral bi-axial AgNS array, an increase of *n* from 0 to 1 eventually renders the UV chiroptical mode blueshift (Fig. 6c) and switch the CD sign (Fig. 6d). The evolution of the visible mode appears to be more complicated than that of the UV mode. When *n* is increased to 2/3, the single-peak visible mode starts to split into two bisignated peaks. The chiroptical response in the 380-500 nm eventually switches the CD sign (e.g. at the wavelength of 450 nm, Fig. 6e). When the heterochiral bi-axial array turns to be co-axial (Fig. 7), the fractional-pitch growth eventually causes the UV mode locate at ~360 nm (Fig. 8a) and switch the CD sign (Figs. 8b-c). The visible mode appears to split into two bisignated peaks in the initial growing stage (*n*: from 0 to 1/3, Fig. 7). Hence, the visible chiroptical mode is divided into the V1 and V2 modes (Fig. 8i). Both the V1 and V2 modes tend to redshift with increasing *n* (Fig. 8d and 8g), and maximize the chiroptical activity at *n* of 2/3 (Figs. 8e, 8f and 8h).

The change in the hetero-axial alignment doesn't affect the *n*-induced chiroptical evolution of the UV mode (as illuminated by the green and red vertical arrows in the UV regime, Figs. 6a-

b versus Figs. 7a-b) but causes a significant difference in that of the visible mode, further illustrating the wavelength-related chiroptical distinction. It is intriguing to find out in the heterochiral bi-axial arrays that chiroptical activity is remarkably quenched in the spectrum of 300-700 nm at *n* of 1/3 and nearly extinct in 300-500 nm at *n* of 2/3, but the UV-visible chiroptical response is evoked while increasing *n* from 2/3 to 1. When the heterochiral bi-axial array becomes co-axial, there is no chiroptical extinction with the evolution of *n*, except that the UV chiroptical response is roughly eliminated at *n* of 1/3 (Figs. 8b-c).

Conclusions

An AgNS array with a helical pitch of ~200 nm is deposited on a UV-visible transparent substrate by GLAD, exhibiting the wavelength-related chiroptical distinction. For the homochiral co-axial array, the UV chiroptical mode is irrelevant to the full-pitch growth (*n*: 1, 2, 3), in terms of the resonance CD wavelength and *n*-normalized ellipticity. On the contrary, the full-pitch growth causes the visible mode significantly quench in the *n*-normalized ellipticity and split into two bisignated modes, of which the one with the shorter resonance wavelength has a blue shift with the helical growth. The FEM simulation together with the LC circuit model illuminates that the wavelength-related chiroptical distinction stems from the difference in optical interaction. The UV irradiation is mainly absorbed in the metal, but the visible is preferentially scattered by AgNSs. For the heterochiral array, chiroptical activity can be effectively tailored in the sign, amplitude and resonance wavelength of CD, via the fractional-pitch growth of the upper spiral (*n*: 1/3, 2/3, 1) and the control over the alignment of the two hetero-helix longitudinal axes. The change in the hetero-axial alignment has little effect on the *n*-induced evolution of the UV chiroptical mode but remarkably alters that of the visible mode, further illustrating the wavelength-related chiroptical distinction.

The facile sculpture in helical structures and handedness via GLAD leads to broadening the horizons in understanding and tailoring the chiroptical activity, which is of vital interest in exploring a wide range of optical applications. For instance, a heterochiral bi-axial AgNS array can function as a circular polarizer in the visible spectrum, simply triggered by either inverting the direction of optical incidence or flipping the array under a given optical incidence. The latter approach is practically preferential in the design of optical devices and superior to the method of switching two homochiral AgNS arrays that are mirror images of one another, since the usage of only one array can significantly reduce the device dimension and cost.

Acknowledgements

The authors gratefully acknowledge Dr. Daniel W. J. Kwong and Ms. Anna O. Y. Chan (Chemistry, HKBU) for their technical support in CD, Mr. F. Bai and Mr. W. F. Lau (Physics, HKBU) for their technical support in GLAD, and financial support by NSFC/21473149 (J.H.D.), HKBU8/CRF/11E (GLAD), SKLP_14-15_P004 (J.H.D.), FRG2/13-14/018 (J.H.D.), NSFC/11304260 (J.N.) and FRG2/13-14/081 (J.H.D., J.N.).

References

1. X. L. Wu, L. G. Xu, L. Q. Liu, W. Ma, H. H. Yin, H. Kuang, L. B. Wang, C. L. Xu and N. A. Kotov, *J. Am. Chem. Soc.*, 2013, **135**, 18629-18636.
2. A. Ben-Moshe, B. Maoz, A. O. Govorov and G. Markovich, *Chem. Soc. Rev.*, 2013, **42**, 7028-7041.
3. N. Berova, L. Di Bari and G. Pescitelli, *Chem. Soc. Rev.*, 2007, **36**, 914-931.
4. T. G. Schaaff and R. L. Whetten, *J. Phys. Chem. B*, 2000, **104**, 2630-2641.
5. I. Lieberman, G. Shemer, T. Fried, E. M. Kosower and G. Markovich, *Angew. Chem.-Int. Edit.*, 2008, **47**, 4855-4857.
6. B. M. Maoz, Y. Chaikin, A. B. Tesler, O. Bar Elli, Z. Y. Fan, A. O. Govorov and G. Markovich, *Nano Lett.*, 2013, **13**, 1203-1209.
7. I. Dolamic, S. Knoppe, A. Dass and T. Burgi, *Nat. Commun.*, 2012, **3**, 798.
8. Z. N. Zhu, W. J. Liu, Z. T. Li, B. Han, Y. L. Zhou, Y. Gao and Z. Y. Tang, *ACS Nano*, 2012, **6**, 2326-2332.
9. A. Kuzyk, R. Schreiber, H. Zhang, A. O. Govorov, T. Liedl and N. Liu, *Nat. Mater.*, 2014, **13**, 862-866.
10. R. Kobayashi, Y. Nonoguchi, A. Sasaki and H. Yao, *J. Phys. Chem. C*, 2014, **118**, 15506-15515.
11. M. Farrag, M. Tschurl and U. Heiz, *Chem. Mater.*, 2013, **25**, 862-870.
12. X. Wu, L. Xu, L. Liu, W. Ma, H. Yin, H. Kuang, L. Wang, C. Xu and N. A. Kotov, *J. Am. Chem. Soc.*, 2013, **135**, 18629-18636.
13. J. Yeom, B. Yeom, H. Chan, K. W. Smith, S. Dominguez-Medina, J. H. Bahng, G. P. Zhao, W. S. Chang, S. J. Chang, A. Chuvilin, D. Melnikau, A. L. Rogach, P. J. Zhang, S. Link, P. Kral and N. A. Kotov, *Nat. Mater.*, 2015, **14**, 66-72.
14. Y. L. Zhou, Z. N. Zhu, W. X. Huang, W. J. Liu, S. J. Wu, X. F. Liu, Y. Gao, W. Zhang and Z. Y. Tang, *Angew. Chem.-Int. Edit.*, 2011, **50**, 11456-11459.
15. S. D. Elliott, M. P. Moloney and Y. K. Gun'ko, *Nano Lett.*, 2008, **8**, 2452-2457.
16. A. Kuzyk, R. Schreiber, Z. Y. Fan, G. Pardatscher, E. M. Roller, A. Hogele, F. C. Simmel, A. O. Govorov and T. Liedl, *Nature*, 2012, **483**, 311-314.
17. C. Y. Song, M. G. Blaber, G. P. Zhao, P. J. Zhang, H. C. Fry, G. C. Schatz and N. L. Rosi, *Nano Lett.*, 2013, **13**, 3256-3261.
18. X. Lan, X. X. Lu, C. Q. Shen, Y. G. Ke, W. H. Ni and Q. B. Wang, *J. Am. Chem. Soc.*, 2015, **137**, 457-462.
19. Z. Chen, X. Lan, Y. C. Chiu, X. X. Lu, W. H. Ni, H. W. Gao and Q. B. Wang, *ACS Photonics*, 2015, **2**, 392-397.
20. X. Lan, Z. Chen, G. L. Dai, X. X. Lu, W. H. Ni and Q. B. Wang, *J. Am. Chem. Soc.*, 2013, **135**, 11441-11444.
21. A. Querejeta-Fernandez, G. Chauve, M. Methot, J. Bouchard and E. Kumacheva, *J. Am. Chem. Soc.*, 2014, **136**, 4788-4793.
22. M. Hentschel, M. Schaferling, T. Weiss, N. Liu and H. Giessen, *Nano Lett.*, 2012, **12**, 2542-2547.

23. Y. Zhao, M. A. Belkin and A. Alu, *Nat. Commun.*, 2012, **3**, 870.
24. Y. Cui, L. Kang, S. Lan, S. Rodrigues and W. Cai, *Nano Lett.*, 2014, **14**, 1021-1025.
25. M. Decker, R. Zhao, C. M. Soukoulis, S. Linden and M. Wegener, *Opt. Lett.*, 2010, **35**, 1593-1595.
26. E. Hendry, T. Carpy, J. Johnston, M. Popland, R. V. Mikhaylovskiy, A. J. Lapthorn, S. M. Kelly, L. D. Barron, N. Gadegaard and M. Kadodwala, *Nat. Nanotechnol.*, 2010, **5**, 783-787.
27. S. Zhang, J. F. Zhou, Y. S. Park, J. Rho, R. Singh, S. Nam, A. K. Azad, H. T. Chen, X. B. Yin, A. J. Taylor and X. Zhang, *Nat. Commun.*, 2012, **3**, 942.
28. E. Plum, J. Zhou, J. Dong, V. A. Fedotov, T. Koschny, C. M. Soukoulis and N. I. Zheludev, *Phys. Rev. B*, 2009, **79**.
29. J. K. Gansel, M. Thiel, M. S. Rill, M. Decker, K. Bade, V. Saile, G. von Freymann, S. Linden and M. Wegener, *Science*, 2009, **325**, 1513-1515.
30. A. G. Mark, J. G. Gibbs, T. C. Lee and P. Fischer, *Nat. Mater.*, 2013, **12**, 802-807.
31. Y. J. Yan, M. I. Rashad, E. J. Teo, H. Tanoto, J. H. Teng and A. A. Bettiol, *Opt. Mater. Express*, 2011, **1**, 1548-1554.
32. J. Hung, W. S. Gao and W. Y. Tam, *J. Opt.*, 2011, **13**, 095102.
33. J. G. Gibbs, A. G. Mark, T. C. Lee, S. Eslami, D. Schamel and P. Fischer, *Nanoscale*, 2014, **6**, 9457-9466.
34. B. Frank, X. H. Yin, M. Schaferling, J. Zhao, S. M. Hein, P. V. Braun and H. Giessen, *ACS Nano*, 2013, **7**, 6321-6329.
35. M. Esposito, V. Tasco, F. Todisco, A. Benedetti, D. Sanvitto and A. Passaseo, *Adv. Opt. Mater.*, 2014, **2**, 154-161.
36. K. Hoflich, R. B. Yang, A. Berger, G. Leuchs and S. Christiansen, *Adv. Mater.*, 2011, **23**, 2657-2661.
37. Z. F. Huang, K. D. Harris and M. J. Brett, *Adv. Mater.*, 2009, **21**, 2983-2987.
38. M. J. Brett and M. M. Hawkeye, *Science*, 2008, **319**, 1192-1193.
39. K. Robbie, M. J. Brett and A. Lakhtakia, *Nature*, 1996, **384**, 616.
40. K. Robbie, D. J. Broer and M. J. Brett, *Nature*, 1999, **399**, 764-766.
41. J. G. Gibbs, A. G. Mark, S. Eslami and P. Fischer, *Appl. Phys. Lett.*, 2013, **103**, 213101.
42. G. K. Larsen and Y. Zhao, *Appl. Phys. Lett.*, 2014, **105**, 071109.
43. J. M. Caridad, D. McCloskey, J. F. Donegan and V. Krstic, *Appl. Phys. Lett.*, 2014, **105**, 233114.
44. J. K. Gansel, M. Wegener, S. Burger and S. Linden, *Opt. Express*, 2010, **18**, 1059-1069.
45. Z. Y. Zhang and Y. P. Zhao, *J. Appl. Phys.*, 2008, **104**, 013517.
46. J. B. Lassiter, H. Sobhani, J. A. Fan, J. Kundu, F. Capasso, P. Nordlander and N. J. Halas, *Nano Lett.*, 2010, **10**, 3184-3189.
47. B. Luk'yanchuk, N. I. Zheludev, S. A. Maier, N. J. Halas, P. Nordlander, H. Giessen and C. T. Chong, *Nat. Mater.*, 2010, **9**, 707-715.
48. M. M. Hawkeye and M. J. Brett, *J. Vac. Sci. Technol. A-Vac. Surf. Films*, 2007, **25**, 1317-1335.

Nanoscale

ARTICLE

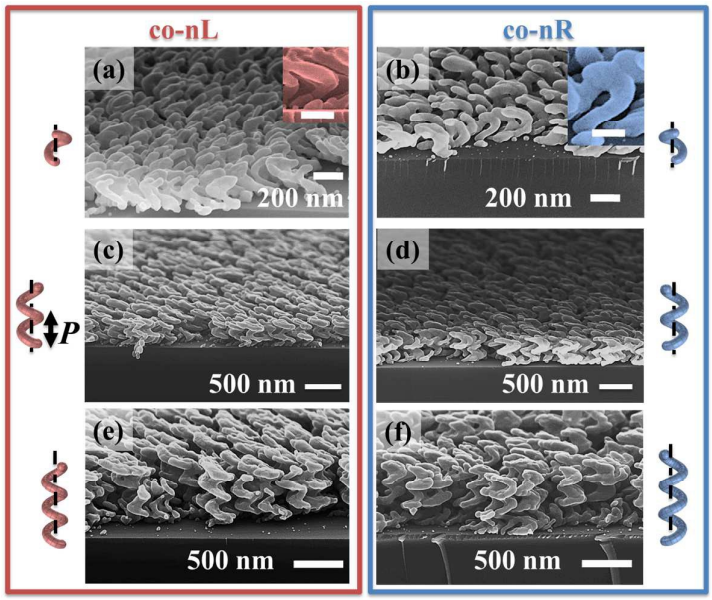

Fig. 1 GLAD of homochiral co-axial (i.e., co-) AgNS arrays, with left (L: a, c, e) and right (R: b, d, f) handedness. AgNSs have helical pitch (*P*) of ~200 nm, and the number of pitch (*n*) is 1 (a, b), 2 (c, d) and 3 (e, f). (a-f) SEM tilted-viewing images of the homochiral co-axial AgNS arrays. Insets in (a, b) are SEM tilted-viewing images to highlight the as-deposited nanostructures, with a scale bar of 100 nm. Each sample is depicted by a corresponding schematic helix. The L- and R-handed AgNSs are represented by red and blue helices, respectively.

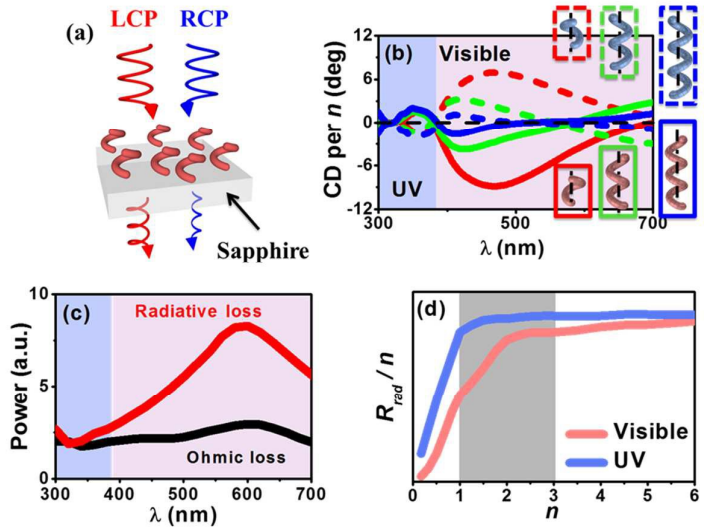

Fig. 2 Chiroptical activity of homochiral co-axial AgNS arrays. (a) Schematic of CD measurement. (b) CD spectra of co-nL and co-nR arrays (*n* of 1, 2 and 3) deposited on sapphires. CD amplitude is normalized by *n*. The blue and pink backgrounds highlight the UV and visible modes, respectively. (c) FEM simulation of radiative and Ohmic loss of a homochiral co-2L AgNS, under LCP incidence and along the helix longitudinal axis. (d) A plot of R_{rad}/n versus *n* for the UV (λ of ~350 nm) and visible (λ: 650-400 nm, blue shift with an increase of *n*) CD modes. R_{rad} is the radiative resistance. The two curves have different scales of unit.

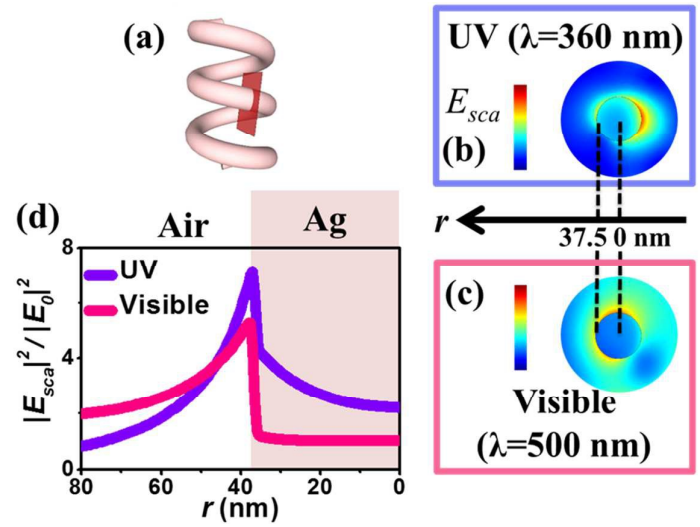

Fig. 3 (a) Schematic of a homochiral co-3L AgNS intersected by a red sheet, under LCP incidence and along the helix longitudinal axis. The distribution of E_{sca} (scattering electric field) in the red sheet, with λ of (b) 360 nm (UV) and (c) 500 nm (visible). (d) A plot of $|E_{sca}|^2$ per $|E_0|^2$ versus r (the radial axis pointing from the center of the red sheet, as inset in (b, c)). The area of the air and AgNS is denoted by r>37.5 nm and r<37.5 nm, respectively. $|E_{sca}|^2$ is the circumferentially integrated intensity as function of r. E_0 is the incident electric field.

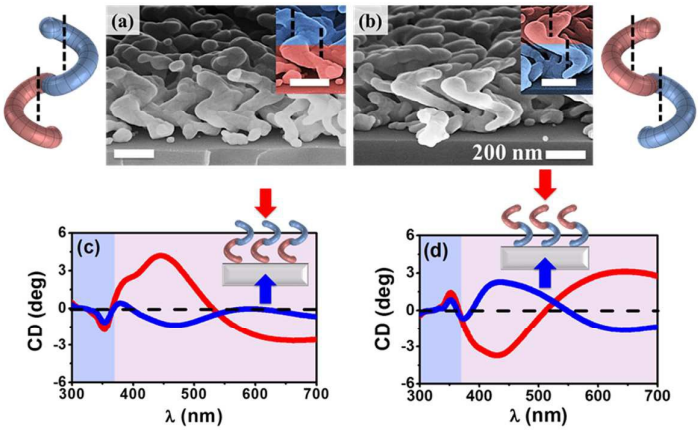

Fig. 4 Chiroptical activity of heterochiral bi-axial (i.e., bi-) AgNS arrays, as function of the direction of optical incidence. SEM tilted-viewing images: (a) bi-(1L+1R); (b) bi-(1R+1L). Insets: schematics and SEM images depict the as-deposited heterochiral structures. All the scale bars represent 200 nm. CD spectra of a heterochiral bi-axial array deposited on a sapphire: (c) bi-(1L+1R), (d) bi-(1R+1L). As shown in the inset schematics, the red and blue spectra are detected under the frontward and backward incidence, respectively.

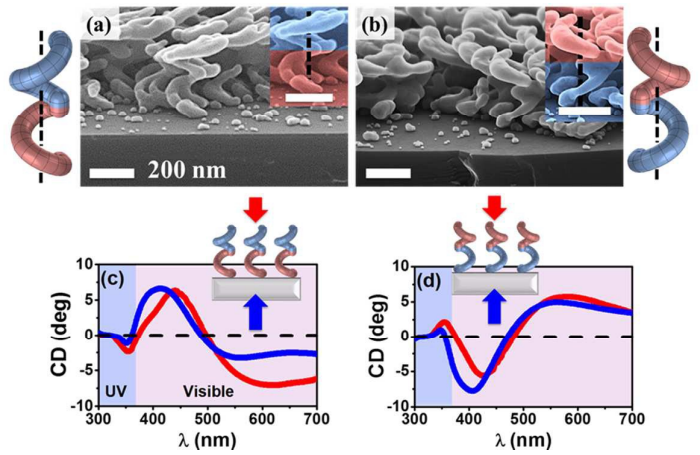

Fig. 5 Chiroptical activity of heterochiral co-axial AgNS arrays, as function of the direction of optical incidence. SEM tilted-viewing images: (a) co-(1L+1R); (b) co-(1R+1L). Insets: schematics and SEM images depict the as-deposited heterochiral structures. All the scale bars represent 200 nm. CD spectra of a heterochiral co-axial AgNS array deposited on a sapphire: (c) co-(1L+1R), (d) co-(1R+1L). As shown in the inset schematics, the red and blue spectra are detected under the frontward and backward incidence, respectively.

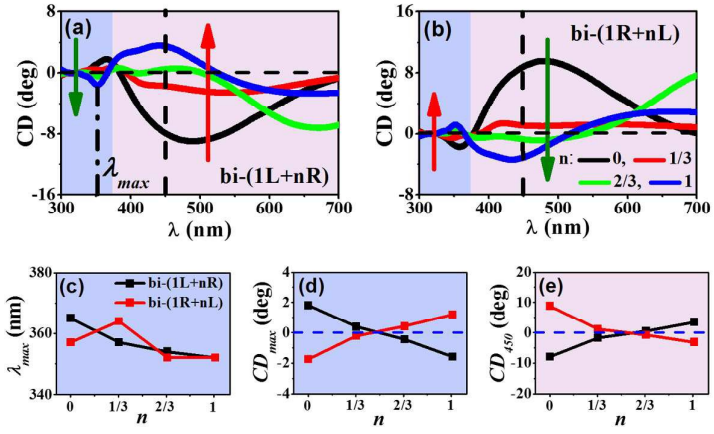

Fig. 6 Chiroptical evolution of heterochiral bi-axial AgNS arrays: (a) bi-(1L+nR); (b) bi-(1R+nL), with *n* of 0, 1/3, 2/3 and 1. The plot (a) has a legend same as that of (b). For the UV mode, a plot of (c) λ_{max} and (d) CD_{max} versus *n*. CD_{max} is the maximum ellipticity at the wavelength of λ_{max}, as shown in (a). (e) A plot of CD_{450} (CD amplitude at the wavelength of 450 nm) versus *n*. The plots (d, e) have a legend same as that of (c).

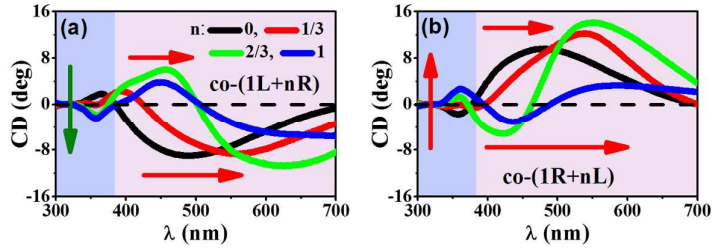

Fig. 7 Chiroptical evolution of heterochiral co-axial AgNS arrays: (a) co-(1L+nR); (b) co-(1R+nL), with *n* of 0, 1/3, 2/3 and 1. The plot (b) has a legend same as that of (a).

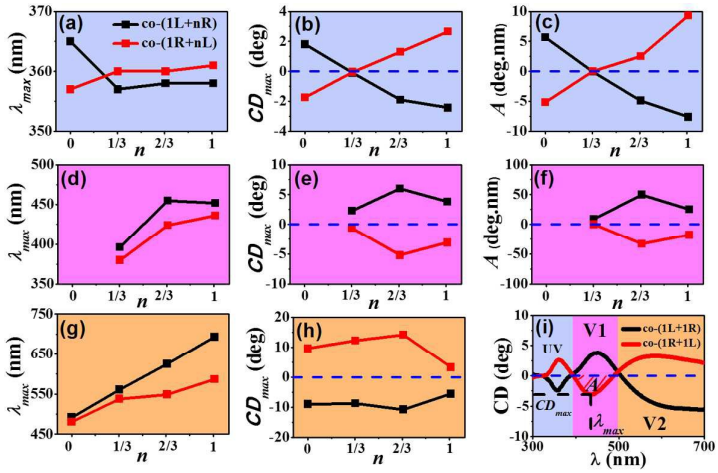

Fig. 8 Quantitative analysis in the CD evolution of heterochiral co-axial AgNSs (Fig. 7): co-(1L+nR) (black squares) and co-(1R+nL) (red squares). (i) CD spectra of co-(1L+1R) and co-(1R+1L) arrays are composed of UV, V1 and V2 modes, marked in blue, magenta, orange backgrounds, respectively. A CD peak can be characterized by the maximum amplitude (CD_{max}) at the wavelength of λ_{max} and an integrated area *A*. (a, d, g): the plots of λ_{max} versus *n*; (b, e, h): the plots of CD_{max} versus *n*; (c, f): the plots of *A* versus *n*. (a-c): the UV mode; (d-f) the V1 mode; (g, h): the V2 mode. The plots of (b-h) have a legend same as that of (a). The visible mode doesn't bisignatedly split at *n* of 0, and the single peak at *n* of 0 is assigned to be the V2 mode. Hence, there is a missing data point at *n* of 0 in (d-f). The V2 mode cannot be fully monitored in 300-700 nm, so that there isn't a plot of *A* versus *n* for the V2 mode.